

Forum

Nanomodulation of Molecular Nanomagnets

Patrick L. Feng,[†] Changhyun Koo,[‡] John J. Henderson,[§] Paul Manning,[†] Motohiro Nakano,^{||} Enrique del Barco,^{*,§} Stephen Hill,^{*,⊥} and David N. Hendrickson^{*,†}

Department of Chemistry and Biochemistry, University of California, San Diego, La Jolla, California 92093-0358, Department of Physics, University of Florida, Gainesville, Florida 32611, Department of Physics, University of Central Florida, Orlando, Florida 32816-2385, Division of Applied Chemistry, Osaka University, Suita, Osaka 565-0871, Japan, and National High Magnetic Field Laboratory and Department of Physics, Florida State University, Tallahassee, Florida 32310

Received December 6, 2008

Detailed synthetic, structural, and magnetic characterizations for a family of six $[\text{Mn}_3\text{Zn}_2]^{13+}$ complexes are presented. These complexes have planar $[\text{Mn}_3^{\text{III}}-(\mu_3\text{-oxo})]^{7+}$ core magnetic units and have formulas represented by $[\text{cation}]_3[\text{Mn}_3\text{Zn}_2(\text{R-salox})_3\text{O}(\text{N}_3)_6\text{X}_2]$, where $[\text{cation}]^+ = [\text{NEt}_4]^+$ or $[\text{AsPh}_4]^+$; $\text{R} = \text{H}$ or Me ; and $\text{X} = \text{Cl}^-$, Br^- , I^- , or N_3^- . Least-squares fits to the magnetic susceptibility data for these complexes indicate large negative values of the axial zero field splitting (ZFS) parameter D (≈ -1.1 K) and spin ground states ranging from a highly spin-mixed $S \approx 1$ to a reasonably isolated $S = 6$ ($\Delta E_{S=5} = 69.2$ K). The strength and magnitude of the intramolecular exchange interactions have been observed to change with the crystal packing as a result of systematic variations in the co-crystallizing cation, terminal ion, and oximate ligand. Alternating current susceptibility data were collected from 1.8–7 K at 10–997 Hz, revealing strong frequency-dependent peaks in the out-of-phase susceptibility (χ''_m) for ferromagnetic $S = 6$ complexes **1**, **2**, and **6**. Fitting of these data to the Arrhenius equation gave $U_{\text{eff}} = 44.0$ K and $\tau_0 = 3.8 \times 10^{-8}$ s for $[\text{NEt}_4]_3[\text{Mn}_3\text{Zn}_2(\text{salox})_3\text{O}(\text{N}_3)_6\text{Cl}_2]$ (**1**), and $U_{\text{eff}} = 45.6$ K and $\tau_0 = 2.1 \times 10^{-7}$ s for $[\text{NEt}_4]_3[\text{Mn}_3\text{Zn}_2(\text{Me-salox})_3\text{O}(\text{N}_3)_6\text{Cl}_2]$ (**6**). The enhanced relaxation behavior in complex **6** is associated with stronger ferromagnetic exchange interactions and a more isolated $S = 6$ ground state than in **1** and **2**. Comprehensive high-frequency electron paramagnetic resonance (HFEP) experiments were conducted on single crystals of complexes **1**, **2**, and **6**, revealing sharp absorption peaks and allowing for the precise determination of ZFS parameters. Similar experiments on $[\text{AsPh}_4]_3[\text{Mn}_3\text{Zn}_2(\text{salox})_3\text{O}(\text{N}_3)_6\text{Cl}_2]$ (**4**) resulted in the observation of a broad absorption peak, consistent with the highly spin-mixed ground state. Single crystal magnetization hysteresis measurements on complexes **1** and **2** indicate SMM behavior via temperature- and sweep-rate dependent hysteresis loops and the observance of very sharp quantum tunneling resonances. Additionally, the Hamiltonian parameters derived from the magnetic data, HFEP, and hysteresis measurements are in good agreement and highlight the relationships between superexchange, spin–orbit interactions, and the varied relaxation behavior in these complexes.

Introduction

Since the discovery of the first single-molecule magnet (SMM) $[\text{Mn}_{12}\text{O}_{12}(\text{CH}_3\text{COO})_{16}(\text{H}_2\text{O})_4] \cdot 2\text{CH}_3\text{COOH} \cdot 4\text{H}_2\text{O}$,

“ $\text{Mn}_{12}\text{—OAc}$ ”, much attention has been directed toward the synthesis and characterization of polynuclear complexes containing anisotropic paramagnetic ions. SMM behavior is due to the intrinsic, intramolecular properties of these compounds and is the result of the combination of a large ground-state spin (S) value and a significant uniaxial (Ising) magnetic anisotropy, as indicated by a negative value of the axial zero-field splitting (ZFS) parameter, D .^{1–3} A SMM is thus characterized as having a significant barrier to reversal of the magnetization vector, with the upper limit to this barrier (U) approximated by $S^2|D|$ and

* To whom correspondence should be addressed. E-mail: dhendrickson@ucsd.edu (D.N.H.), shill@magnet.fsu.edu (S.H.), delbarco@physics.ucf.edu (E.d.B.).

[†] University of California, San Diego.

[‡] University of Florida.

[§] University of Central Florida.

^{||} Osaka University.

[⊥] Florida State University.

$(S^2 - 1/4)|D|$ for integer and half-integer S values, respectively. This barrier results in out-of-phase alternating current (ac) susceptibility signals (χ''_M) and hysteresis loops in magnetization versus applied direct current (dc) field sweeps. Magnetization hysteresis loops for SMMs also indicate the confluence of classical and quantum behavior, where vertical steps indicate quantum tunneling of the magnetization (QTM) through the thermodynamic anisotropy barrier. As a result, SMMs represent a molecular approach to nanoscale magnets, and differ considerably from classical nanoscale magnetic materials. Most important among these differences are an SMM's monodispersity, crystallinity, and minimization of intermolecular interactions via diamagnetic ligands.

The majority of SMMs are based on high-spin Mn^{III} ions, as clusters containing Mn^{III} often exhibit large spin ground-state values (S) and an appreciable negative axial ZFS (D). Among these structures are manganese complexes ranging in nuclearity from 3 to 84, from which interesting phenomena such as QTM, exchange bias, and quantum phase interference have been observed.^{4–11} Most of these results have been driven by the search for a “better SMM”, where higher spin ground states and larger D -values represent the primary goal. Other studies have focused on the systematic construction of SMM families, where detailed comparisons between related complexes have been invaluable. This was first employed in the one- and two-electron reduction products of the $[\text{Mn}_{12}\text{O}_{12}(\text{RCOO})_{16}(\text{H}_2\text{O})_4]$ family and resulted in closely related SMMs with integer and half-integer spin ground states, respectively.^{12–14} This allowed for spin-parity dependent comparisons to be made with respect

Table 1. Molecular Formulae for Complexes 1–6

complex	molecular formula
1	$[\text{NEt}_4]_3[\text{Mn}_3\text{Zn}_2(\text{salox})_3\text{O}(\text{N}_3)_6\text{Cl}_2]$
2	$[\text{NEt}_4]_3[\text{Mn}_3\text{Zn}_2(\text{salox})_3\text{O}(\text{N}_3)_6\text{Br}_2]$
3	$[\text{NEt}_4]_3[\text{Mn}_3\text{Zn}_2(\text{salox})_3\text{O}(\text{N}_3)_8] \cdot \text{MeOH}$
4	$[\text{AsPh}_4]_3[\text{Mn}_3\text{Zn}_2(\text{salox})_3\text{O}(\text{N}_3)_6\text{Cl}_2]$
5	$[\text{NEt}_4]_3[\text{Mn}_3\text{Zn}_2(\text{salox})_3\text{O}(\text{N}_3)_6\text{I}_2] \cdot 2\text{MeOH}$
6	$[\text{NEt}_4]_3[\text{Mn}_3\text{Zn}_2(\text{Me-salox})_3\text{O}(\text{N}_3)_6\text{Cl}_2]$

to the magnetization quantum tunneling in these complexes. The $S = 9/2$ $\text{Mn}_3^{\text{III}}\text{Mn}^{\text{IV}}$ cubane family has also been studied in detail.^{4,10,11,15,16} These studies were significant because a few of the complexes showed HFEPR spectra and magnetization hysteresis loops that were quite different from the other members of this family. Close inspection of the crystalline structure revealed hydrogen bonding interactions between nearest $\text{Mn}_3^{\text{III}}\text{Mn}^{\text{IV}}$ neighbors, resulting in a quantum-mechanically coupled $[\text{Mn}_3^{\text{III}}\text{Mn}^{\text{IV}}]_2$ dimer.¹¹ The intermolecular interactions were found to directly account for the spectroscopic and magnetic data and, for the first time, provided insights into coherence associated with the spin states of quantum mechanically coupled SMMs.^{10,11} More recently, the phenomenon of quantum phase interference has been explored in a family of $[\text{Mn}_{12}(\text{X-dea})_8(\text{RCOO})_{14}]$ wheels, where $\text{X-deaH}_2 = \text{N-allyl diethanolamine}$ or $\text{N-ethyl diethanolamine}$, and $\text{RCOO}^- = \text{acetate}$, propionate.^{17,18} While the majority of these wheels may be described by a single $S = 7$ spin ground state, others showed anomalous resonances in single-crystal magnetization hysteresis experiments. Closer inspection of the structures and hysteresis data indicate weakened ferromagnetic interactions between the two $S = 7/2$ halves of the wheel, resulting in a Berry phase effect arising from quantum interference of the two tunneling paths.

Here we present the magnetic and relaxation behavior for a family of complexes based on a triangular Mn_3^{III} magnetic unit. Although Mn_3^{III} triangles have been known for some time, there has been renewed synthetic and theoretical interest in these complexes, as ferromagnetic examples have only recently been realized. Almost all of these ferromagnetic complexes are similar in that they feature three tridentate oximate ligands and an out-of-plane μ_3 -oxo group.^{19,20} Our $[\text{Mn}_3\text{Zn}_2]^{13+}$ complexes exhibit a trigonal bipyramidal structure, where the magnetic core is composed of a planar $\text{Mn}_3^{\text{III}}-(\mu_3\text{-oxo})$ triangle. Methodical changes in the co-crystallizing cation, coordinating oximate ligand, or terminal ion result in significant changes to the sign and magnitude of the observed magnetic exchange interactions. These synthetic variations are evident in the molecular formulas for these complexes, as summarized in Table 1, Figures 1 and 2, and described in the synthesis section below. Additionally, comparisons of ac susceptibility data indicate the relaxation

- (1) Sessoli, R.; Tsai, H. L.; Schake, A. R.; Wang, S. Y.; Vincent, J. B.; Folting, K.; Gatteschi, D.; Christou, G.; Hendrickson, D. N. *J. Am. Chem. Soc.* **1993**, *115*, 1804–1816.
- (2) Sessoli, R.; Gatteschi, D.; Caneschi, A.; Novak, M. A. *Nature* **1993**, *365*, 141–143.
- (3) Christou, G.; Gatteschi, D.; Hendrickson, D. N.; Sessoli, R. *MRS Bull.* **2000**, *25*, 66–71.
- (4) Aubin, S. M. J.; Dille, N. R.; Pardi, L.; Krzystek, J.; Wemple, M. W.; Brunel, L. C.; Maple, M. B.; Christou, G.; Hendrickson, D. N. *J. Am. Chem. Soc.* **1998**, *120*, 4991–5004.
- (5) Aubin, S. M. J.; Wemple, M. W.; Adams, D. M.; Tsai, H. L.; Christou, G.; Hendrickson, D. N. *J. Am. Chem. Soc.* **1996**, *118*, 7746–7754.
- (6) Stamatatos, T. C.; Foguet-Albiol, D.; Stoumpos, C. C.; Raptopoulou, C. P.; Terzis, A.; Wernsdorfer, W.; Perlepes, S. P.; Christou, G. *J. Am. Chem. Soc.* **2005**, *127*, 15380–15381.
- (7) Brechin, E. K.; Sanudo, E. C.; Wernsdorfer, W.; Boskovic, C.; Yoo, J.; Hendrickson, D. N.; Yamaguchi, A.; Ishimoto, H.; Concolino, T. E.; Rheingold, A. L.; Christou, G. *Inorg. Chem.* **2005**, *44*, 502–511.
- (8) Wernsdorfer, W.; Bhaduri, S.; Boskovic, C.; Christou, G.; Hendrickson, D. N. *Phys. Rev. B* **2002**, *65*, 180403.
- (9) Wernsdorfer, W.; Bhaduri, S.; Tiron, R.; Hendrickson, D. N.; Christou, G. *Phys. Rev. Lett.* **2002**, *89*, 197201.
- (10) Wernsdorfer, W.; Aliaga-Alcalde, N.; Hendrickson, D. N.; Christou, G. *Nature* **2002**, *416*, 406–409.
- (11) Hill, S.; Edwards, R. S.; Aliaga-Alcalde, N.; Christou, G. *Science* **2003**, *302*, 1015–1018.
- (12) Aubin, S. M. J.; Sun, Z. M.; Pardi, L.; Krzystek, J.; Folting, K.; Brunel, L. C.; Rheingold, A. L.; Christou, G.; Hendrickson, D. N. *Inorg. Chem.* **1999**, *38*, 5329–5340.
- (13) Kuroda-Sowa, T.; Nakano, M.; Christou, G.; Hendrickson, D. N. *Polyhedron* **2001**, *20*, 1529–1536.
- (14) Soler, M.; Wernsdorfer, W.; Abboud, K. A.; Huffman, J. C.; Davidson, E. R.; Hendrickson, D. N.; Christou, G. *J. Am. Chem. Soc.* **2003**, *125*, 3576–3588.
- (15) Aliaga-Alcalde, N.; Edwards, R. S.; Hill, S. O.; Wernsdorfer, W.; Folting, K.; Christou, G. *J. Am. Chem. Soc.* **2004**, *126*, 12503–12516.
- (16) Hendrickson, D. N.; Christou, G.; Schmitt, E. A.; Libby, E.; Bashkin, J. S.; Wang, S. Y.; Tsai, H. L.; Vincent, J. B.; Boyd, P. D. W.; Huffman, J. C.; Folting, K.; Li, Q. Y.; Streib, W. E. *J. Am. Chem. Soc.* **1992**, *114*, 2455–2471.

- (17) Shah, S. J.; Ramsey, C. M.; Heroux, K. J.; DiPasquale, A. G.; Dalal, N. S.; Rheingold, A. L.; del Barco, E.; Hendrickson, D. N. *Inorg. Chem.* **2008**, *47*, 9569–9582.
- (18) Ramsey, C. M.; del Barco, E.; Hill, S.; Shah, S. J.; Beedle, C. C.; Hendrickson, D. N. *Nature Phys.* **2008**, *4*, 277–281.
- (19) Viciano-Chumillas, M.; Tanase, S.; Mutikainen, I.; Turpeinen, U.; Jos de Jongh, L.; Reedijk, J. *Inorg. Chem.* **2008**, *47*, 5919–5929.
- (20) Stamatatos, T. C.; Foguet-Albiol, D.; Lee, S. C.; Stoumpos, C. C.; Raptopoulou, C. P.; Terzis, A.; Wernsdorfer, W.; Hill, S. O.; Perlepes, S. P.; Christou, G. *J. Am. Chem. Soc.* **2007**, *129*, 9484–9499.

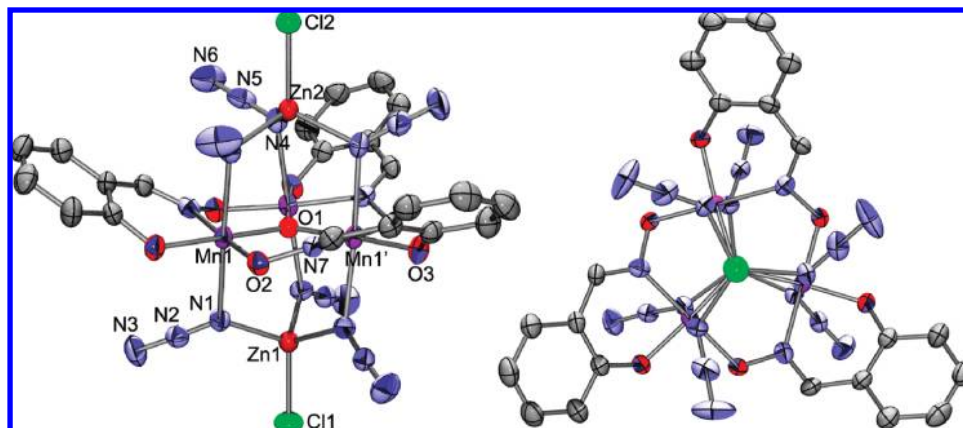


Figure 1. ORTEP representations of complex **1**, viewed near the *a-b* plane (left) and along the *c*-axis (right). Ellipsoids are shown at the 50% probability level, and $[\text{NEt}_4]^+$ cations have been omitted for clarity.

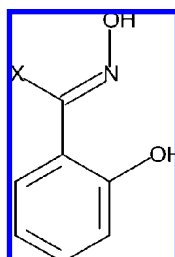


Figure 2. Structure of saloxH_2 ($X = \text{H}$) and Me-saloxH_2 ($X = \text{Me}$).

effects associated with changes in the strength of the magnetic exchange interactions. Thus, we describe here the significant changes in magnetic properties and magnetization dynamics associated with the chemical modulation of coordinating ligands and co-crystallizing cations. Portions of this work have been previously communicated.²¹

Experimental Section

Physical Measurements. Elemental analyses were performed by NuMega Resonance Laboratories (San Diego, CA) for complexes **1–6**. Direct current magnetic susceptibility measurements employed finely ground polycrystalline samples of complexes **1–6** that were restrained in eicosane to prevent torquing of the microcrystallites in the externally applied magnetic field. The measurements were performed using a Quantum Design MPMS-5 magnetometer equipped with a 5.5 T magnet in the 1.8–300 K temperature range with applied fields of 0.1–50 kG. Alternating current magnetic susceptibility measurements were obtained between 1 and 7 K with a 3 G ac field at frequencies in the range of 10–997 Hz with zero applied dc magnetic field using a Quantum Design MPMS-2 magnetometer. Data were corrected for diamagnetic contributions resulting from the sample rod, the capsule, and eicosane. Corrections for diamagnetism were estimated from Pascal's constants, yielding the overall paramagnetic contribution to the molar magnetic susceptibility. Single-crystal HFEP data were collected using a millimeter-wave vector network analyzer (MVNA) and a high-sensitivity cavity perturbation technique described elsewhere.^{22,23} Single-crystal magnetization hysteresis measurements were performed in a Oxford Instruments He³ cryostat

at temperatures ranging from 0.3–2.3 K and magnetic fields (<8 T) generated by a vector superconducting magnet. The crystals were glued with vacuum grease to the surface of a high-sensitivity micro-Hall effect magnetometry sensor based on AlGaAs-GaAs 2DEG heterostructure.

X-ray Crystallography. Diffraction intensity data were collected at -173°C for complexes **1–6**. A Bruker Smart Apex CCD diffractometer was used, and the resulting data were integrated using the Bruker SAINT software program and corrected for absorption using the Bruker SADABS program. Crystal data, data collection, and refinement parameters for complexes **1–6** are given in Table 2. The structures of complexes **1–6** were solved by direct methods (SHELXS-97), developed by successive difference Fourier syntheses, and refined by full-matrix least-squares on all F^2 data. All non-hydrogen atoms were refined anisotropically, and hydrogen atoms were placed in calculated positions with temperature factors fixed at 1.2 times the equivalent isotropic U values for the C atoms to which they were bonded. To account for unresolved solvent and disordered counter-ions in complex **5**, the PLATON program SQUEEZE was used; it found 1247 electrons per unit cell, or 3 molecules of NEt_4^+ and 2 molecules of methanol (199 electrons per molecule) per molecular unit. Solvent electron density was therefore included in the molecular formula of **5** as 2MeOH .

Materials and Synthesis. All manipulations were performed under aerobic conditions using commercial reagents as received, unless otherwise noted. Me-saloxH₂ was synthesized according to literature procedures.²⁴ **Warning!** Azide salts are very toxic and potentially explosive. Although no problems were encountered in this work, these materials should be synthesized in small quantities and handled with extreme care.

$[\text{NEt}_4]_3[\text{Mn}_3\text{Zn}_2(\text{salox})_3\text{O}(\text{N}_3)_6\text{Cl}_2]$ (1**).** Sodium azide (0.26 g, 4.00 mmol) and salicylaldehyde (0.28 g, 2.07 mmol) were added to a stirring methanol solution (125 mL) of $\text{MnCl}_2 \cdot 4\text{H}_2\text{O}$ (0.40 g, 2.02 mmol) and ZnCl_2 (0.28 g, 2.05 mmol). The mixture was stirred for 15 min, after which 0.7 mL of a 20% solution of NEt_4OH (in H_2O) was added. The green solution was stirred for 5 additional minutes, resulting in a green-yellow filtrate and a small amount of shiny green-black precipitate. The filtrate was collected and left undisturbed. After 4 days, numerous trigonal pyramidal crystals formed in high yield (85% based on Mn). Identical IR spectra and elemental analysis results were obtained for the crystals and green-black precipitate. Elemental analysis data for (**1**): Found: C, 38.00%; H, 4.66%; N, 23.43%. Calcd: C, 37.78%; H, 5.28%; N, 23.50%.

(21) Feng, P. L.; Koo, C.; Henderson, J. J.; Nakano, M.; Hill, S.; del Barco, E.; Hendrickson, D. N. *Inorg. Chem.* **2008**, *47*, 8610–8612.

(22) Mola, M.; Hill, S.; Goy, P.; Gross, M. *Rev. Sci. Instrum.* **2000**, *71*, 186–200.

(23) Takahashi, S.; Hill, S. *Rev. Sci. Instrum.* **2005**, *76*, 023114.

(24) Stokker, G. J. *Org. Chem.* **1982**, *48*, 2613–2615.

Table 2. Crystal Data and Structure Refinement Parameters for Compounds **1–6**

compound	1	2	3·MeOH	4	5·2MeOH	6
formula	C ₄₅ H ₇₅ N ₂₄ O ₇ Mn ₃ Zn ₂ Cl ₂	C ₄₅ H ₇₅ N ₂₄ O ₇ Mn ₃ Zn ₂ Br ₂	C ₄₆ H ₇₉ N ₃₀ O ₈ Mn ₃ Zn ₂	As ₃ C ₉₃ H ₇₅ N ₂₁ O ₇ Mn ₃ Zn ₂ Cl ₂	C ₄₇ H ₈₃ N ₂₄ O ₉ Mn ₃ Zn ₂ I ₂	C ₄₈ H ₈₄ N ₂₄ O ₇ Mn ₃ Zn ₂ Cl ₂
fw	1430.73	1519.64	1475.91	2189.99	1677.72	1475.84
cryst syst	trigonal	trigonal	monoclinic	trigonal	monoclinic	trigonal
space grp	<i>R</i> 3c	<i>R</i> 3c	<i>P</i> 2 ₁ / <i>n</i>	<i>R</i> 3c	<i>P</i> 2 ₁ / <i>c</i>	<i>R</i> 3c
<i>a</i> (Å)	13.4536(8)	13.4023(17)	18.1918(9)	20.282(3)	17.199(3)	13.5805(13)
<i>b</i> (Å)	13.4536(8)	13.4023(17)	19.9808(10)	20.282(3)	12.269(2)	13.5805(13)
<i>c</i> (Å)	60.451(7)	60.923(8)	18.4894(9)	83.734(12)	21.095(4)	61.748(6)
α (deg)	90.00	90.00	90.00	90.00	90.00	90.00
β (deg)	90.00	90.00	106.8040(10)	90.00	110.014(2)	90.00
γ (deg)	120.00	120.00	90.00	120.00	90.00	120.00
<i>V</i> (Å ³)	9475.7(14)	9477(2)	6433.7(6)	29830(7)	4182.7(13)	9862.4(17)
<i>Z</i>	6	6	4	12	4	6
<i>T</i> (K)	100(2)	100(2)	100(2)	100(2)	100(2)	100(2)
μ (mm ⁻¹)	1.595	2.666	1.380	1.953	2.255	1.426
<i>D</i> (g cm ⁻³)	1.504	1.626	1.520	1.461	1.737	1.488
<i>F</i> ₀₀₀	4770	4650	3040	13212	2180	4572
refls meas	18864	21402	60710	171334	63801	48251
refls used	3836	3551	11774	5855	7694	3857
<i>R</i> 1 ^a	0.0332	0.0218	0.0417	0.0556	0.0441	0.0526
<i>wR</i> 2 ^b	0.0701	0.0495	0.0871	0.1496	0.0993	0.1436
GOF on <i>F</i> ²	1.023	1.020	0.999	1.076	1.021	1.047

^a *R*1 = $\sum ||F_o| - |F_c|| / \sum |F_o|$ (*I* > 2.00σ(*I*)). ^b *wR*2 = $[\sum w(F_o^2 - F_c^2)^2 / \sum w(F_o^2)]^{1/2}$ (all data).

[NEt₄]₃[Mn₃Zn₂(salox)₃O(N₃)₆Br₂] (**2**). A similar procedure to **1** was followed, except using MnBr₂·4H₂O (0.6 g, 2.09 mmol) and ZnBr₂ (0.3 g, 1.33 mmol) instead. No precipitate formed after stirring, and larger pyramid shaped crystals were obtained in 90% yield after 2 days. Elemental analysis data for (**2**): Found: C, 36.11%; H, 5.13%; N, 22.71%. Calcd: C, 35.57%; H, 4.97%; N, 22.12%.

[NEt₄]₃[Mn₃Zn₂(salox)₃O(N₃)₈] (**3**). Mn(NO₃)₂·4H₂O (0.5 g, 1.99 mmol), Zn(NO₃)₂·6H₂O (0.393 g, 1.32 mmol), and NaN₃ (0.26 g, 1.91 mmol) were added to 30 mL of MeOH and stirred for 1 h. Salicylaldoxime (0.28 g, 2.07 mmol) and 1.0 mL of a 20% solution of NEt₄OH (in H₂O) were added to the clear solution, and the resulting mixture was stirred overnight. Large black block-shaped crystals formed over 2 weeks in 82% yield (based on Mn). Elemental analysis data for (**3**): Found: C, 37.82%; H, 5.59%; N, 27.87%. Calcd: C, 37.43%; H, 5.40%; N, 28.47%.

[AsPh₄]₃[Mn₃Zn₂(salox)₃O(N₃)₆Cl₂] (**4**). A similar procedure to **1** was followed, using Mn(NO₃)₂ (0.50 g, 1.99 mmol), Zn(NO₃)₂ (0.393 g, 1.32 mmol), NaN₃ (0.26 g, 4.00 mmol), salicylaldoxime (0.28 g, 2.07 mmol), NaOH (0.02 g, 5.00 mmol), and AsPh₄Cl (0.846 g, 2.02 mmol) instead. Large olive green trigonal bipyramidal crystals formed over 2 days in 88% yield (based on Mn). Elemental analysis data for (**4**): Found: C, 49.77%; H, 3.57%; N, 13.19%. Calcd: C, 50.03; H, 3.45%; N, 13.43%.

[NEt₄]₃[Mn₃Zn₂(salox)₃O(N₃)₆I₂]·2MeOH (**5**). A similar procedure to **1** was followed, using Mn(NO₃)₂·6H₂O (0.50 g, 1.74 mmol), Zn(NO₃)₂·6H₂O (0.393 g, 1.32 mmol), NaN₃ (0.26 g, 4.00 mmol), salicylaldoxime (0.28 g, 2.07 mmol), NEt₄OH (0.7 mL of a 20% solution in H₂O), and NaI (0.3 g, 2.00 mmol). The NaI was predissolved in 1 mL of H₂O prior to addition. Long green needle-shaped crystals formed from a standing MeOH solution over 3 days in 75% yield (based on Mn). Elemental analysis data for (**5**): Found: C, 32.41%; H, 4.25%; N, 21.25%. Calcd: C, 33.57; H, 4.84%; N, 20.43%.

[NEt₄]₃[Mn₃Zn₂(Me-salox)₃O(N₃)₆Cl₂] (**6**). A similar procedure to **1** was followed, except using Me-salox (0.32 g, 2.13 mmol) and 50 mL of methanol. The dark brown-olive solution was filtered after stirring for 2 h, resulting in a clear filtrate and no precipitate. Green-yellow elongated bipyramidal crystals formed from the standing MeOH solution after 4 days in 71% yield (based on Mn). Elemental analysis data for (**6**): Found: C, 39.00%; H, 5.14%; N, 23.13%. Calcd: C, 39.14; H, 5.54%; N, 22.82%.

Results and Discussion

Comparison of the Structures of 1–6 with Other [Mn^{III}-(μ₃-oxo)]⁷⁺ Complexes. In view of the large number of triangular [Mn^{III}-(μ₃-oxo)]⁷⁺ complexes that have been reported, it is of particular interest to understand which factors govern the nature of magnetic exchange within these basic structures. Most known examples are characterized by antiferromagnetic interactions, resulting in frustrated low-spin ground states. Numerous [Mn₃O(O₂CR)₆L₃]⁺, (L = py, H₂O) complexes have been characterized and have been utilized as starting materials for the synthesis of many other polynuclear manganese structures.^{25–28} Antiferromagnetic exchange interactions in the [Mn₃O(O₂CR)₆(L)₃]⁺ triangles propagate through a virtually planar μ₃-oxo bridging group and through six bridging carboxylate ligands.^{29,30} Isostructural, mixed-valent Mn^{II}Mn^{III} triangles have also been synthesized and well-characterized.^{31,32}

Another, more recent class of triangular [Mn^{III}-(μ₃-oxo)]⁷⁺ complexes include examples that are similar to the aforementioned [Mn₃O(O₂CR)₆L₃]⁺ structures but with carboxylate and L groups replaced by tridentate oximate ligands.^{20,33} These complexes have been of interest because they resulted in the first examples of ferromagnetic triangular Mn^{III} SMMs. The first example is [Mn₃O(salox)₃(O₂CMe)-

- (25) Ribas, J.; Albella, B.; Stoeckli-Evans, H.; Christou, G. *Inorg. Chem.* **1997**, *36*, 2352–2360.
- (26) Scott, R. T. W.; Parsons, S.; Murugesu, M.; Wernsdorfer, W.; Christou, G.; Brechin, E. K. *Angew. Chem.* **2005**, *44*, 6540–6543.
- (27) Manoli, M.; Milios, C. J.; Mishra, A.; Christou, G.; Brechin, E. K. *Polyhedron* **2007**, *26*, 1923–1926.
- (28) Murugesu, M.; Habrych, M.; Wernsdorfer, W.; Abboud, K. A.; Christou, G. *J. Am. Chem. Soc.* **2004**, *126*, 4766–4767.
- (29) Vincent, J. B.; Chang, H. R.; Folting, K.; Huffman, J. C.; Christou, G.; Hendrickson, D. N. *J. Am. Chem. Soc.* **1987**, *109*, 5703–5711.
- (30) Mccusker, J. K.; Jang, H. G.; Wang, S.; Christou, G.; Hendrickson, D. N. *Inorg. Chem.* **1992**, *31*, 1874–1880.
- (31) Nakano, M.; Sorai, M.; Vincent, J. B.; Christou, G.; Ho, G. J.; Hendrickson, D. N. *Inorg. Chem.* **1989**, *28*, 4608–4614.
- (32) Jang, H. G.; Vincent, J. B.; Nakano, M.; Huffman, J. C.; Christou, G.; Sorai, M.; Wittebort, R. J.; Hendrickson, D. N. *J. Am. Chem. Soc.* **1989**, *111*, 7778–7784.
- (33) Sreerama, S. G.; Pal, S. *Inorg. Chem.* **2002**, *41*, 4843–4845.

(H₂O)(py)₃], where saloxH₂ = salicylaldoxime.³⁴ The molecular structure of this complex is characterized by planar bridging salox²⁻ groups and a μ_3 -oxo residing 0.325 Å above the Mn₃ plane. Magnetic measurements on this complex indicate dominant antiferromagnetic interactions corresponding to an $S \approx 2$ spin ground state. A related example is the ferromagnetic $S = 6$ SMM [Mn₃O(O₂CMe)₃(mpko)₃](ClO₄) complex, where mpkoH is methyl-2-pyridyl ketone oxime. Although the out-of-plane displacement of the μ_3 -oxo group is similar to the related $S \approx 2$ complex described above, this complex features a coordinatively different oximate ligand, resulting in an observed twisting of the formerly parallel Mn^{III} JT axes. Projections of the strongly canted individual-ion JT axes lead to a molecular axial ZFS parameter of $D = -0.3$ cm⁻¹ and $U_{\text{eff}} = 10.9$ K. Cano et al.³⁴ have performed density-functional theory (DFT) calculations on these two structures, in an attempt to rationalize the observed change from $S \approx 2$ to $S = 6$. The results from their study suggest that the oxime twist angle, JT axes (mis)alignment, and displacement of the μ_3 -oxo from the Mn₃ plane are all important factors that influence the observed magnetic properties. However, in spite of these interesting results, this study makes comparisons between significantly different Mn₃^{III} complexes. Comparisons between the coordination environments in these two complexes reveal a change from a monoanionic N,N,O-oxime to a dianionic O,N,O-oxime and a switch from one bridging carboxylate to three bridging carboxylate groups. Furthermore, [Mn₃O(salox)₃(O₂CMe)(H₂O)(py)₃] is a neutral molecule while [Mn₃O(O₂CMe)₃(mpko)₃]⁺ is positively charged.

A third example of an oximate-coordinated Mn₃^{III} triangle is the recently reported [Mn₃O(Me-salox)₃(2,4'-bpy)(ClO₄)]·0.5MeCN complex.³⁵ This molecule is similar to the ferromagnetic example above as it retains an out-of-plane μ_3 -oxo group, has twisted oximate ligands (44.15°), and an $S = 6$ spin ground state. In contrast, the JT elongation axes in this complex are significantly less canted than in the example above, leading to a larger axial ZFS parameter and an increased U_{eff} barrier of 37.5 K. It appears, however, that the increased anisotropy has come at a cost; the authors observe weakened ferromagnetic exchange interactions and indicate that hysteresis loop measurements reveal significant QTM through a low-lying excited-state spin manifold.

Triangular [Mn₃^{III}-(μ_3 -oxo)]⁷⁺ are thus of interest not only because of their broad application potential as starting materials but also because of their interesting magnetic properties and structural relationship to larger polynuclear metal clusters. A better understanding of these simple triangles is a prerequisite for understanding the magnetic behavior in more complex structures based on these molecular subunits.

Description of Structures. In the context of the above discussion, we report here the first examples of $S \approx 1$ to $S = 6$ Mn₃^{III} triangles that have planar [Mn₃^{III}-(μ_3 -oxo)]⁷⁺ units and coordinatively identical magnetic cores. Each Mn^{III} ion

has a nearly octahedral coordination geometry and an axial JT distortion, as expected for a high-spin d⁴ ion. The manganese oxidation states were further confirmed as +3 through charge balance considerations and bond valence sum analysis (BVS),³⁶ as shown in Supporting Information, Table S1. The Mn₃^{III} magnetic core in each of these complexes is composed of a central in plane μ_3 -oxo, three bridging oximate ligands, and six axially bound μ - η^1 : η^1 azido- ligands. The Mn–azide bonds lie along the axial JT distortion axis and connect the Mn₃^{III} core to two tetrahedral, nonmagnetic Zn^{II} ions. This coordination environment constrains the axial orientation and canting angle of Mn^{III} JT axes, resulting in almost parallel individual-ion JT axes. It is likely that this bonding arrangement also forces the μ_3 -oxo into the Mn₃ plane, as deviations from planarity would result in increased geometric strain. An out-of-plane μ_3 -oxo would require the JT axes to tilt inward toward the central oxide, thus preventing equivalent coordination sites for Zn^{II} above and below the Mn₃^{III} plane. This expected behavior is confirmed experimentally in the previously reported [Mn₃O(Me-salox)₃(2,4'-bpy)(ClO₄)]·0.5MeCN complex, where the JT axes' projections above and below the buckled [Mn₃^{III}-(μ_3 -oxo)] plane form a cone of increasing diameter. The structural rigidity of complexes **1–6**, compared with the relative coordinative flexibility of previous Mn₃^{III} triangles, likely accounts for the in-plane μ_3 -oxo in our structures.

Although complexes **1–6** each possess the same structural topology and have similar bond connectivities, the observed variations in crystal packing, local symmetry, and ligand geometry lead to large differences in magnetic properties. The C₃-symmetric salicylaldoximate complexes **1** and **2** crystallize in the trigonal space group *R3c* and have virtually identical coordination geometries. The asymmetric unit within each structure contains 1/3 of a unique molecule; application of the *c*- glide plane and C₃ symmetry operations result in an axially symmetric molecular orientation within the solid state packing, as depicted in Supporting Information, Figure S1. The centered μ_3 -oxo in complex **1** lies just 0.029 Å out of the Mn₃^{III} plane, while η^1 : η^1 : η^1 , μ -salox²⁻ ligands bridge neighboring Mn^{III} ions. The non-planar oximate coordination mode in **1** results in a Mn1–N7–O2–Mn1' torsion angle of $\theta = 32.05^\circ$. Variations in this torsion angle have been shown to account for changes in the sign and magnitude of intramolecular exchanges interactions and will be discussed below. The bridging azido- groups lie along the individual-ion JT elongation axes and are canted $\delta = 8.50^\circ$ with respect to the molecular easy-axis in **1**. The tilting of JT axes in this complex may be described by a single torsion angle because of the C₃ symmetry and almost identical Zn^{II} coordination environments above and below the Mn₃^{III} plane. Complex **2** has virtually the same structural parameters, as summarized in Table 3. Complex **6** is essentially isomorphous to **1** and **2**, crystallizing in the same *R3c* space group and with the molecular easy axes aligned with the *c*- crystallographic axis. However, complex **6** differs

(34) Cano, J.; Cauchy, T.; Ruiz, E.; Milios, C. J.; Stoumpos, C. C.; Stamatatos, T. C.; Perlepes, S. P.; Christou, G.; Brechin, E. K. *Dalton Trans.* **2007**, 2, 234–240.

(35) Yang, C.-I.; Wernsdorfer, W.; Cheng, K.-H.; Nakano, M.; Lee, G.-H.; Tsai, H.-L. *Inorg. Chem.* **2008**, 47, 10184–10186.

(36) Brown, I. D.; Altermatt, D. *Acta Crystallogr.* **1985**, B41, 244–247.

Table 3. Selected Structural Parameters for Complexes **1–6**

complex	Mn–N–O–Mn torsion angle (θ , deg)	μ_3 -oxo out-of-plane shift (\AA)	Jahn–Teller torsion angle (δ), (deg)	Mn–Mn distance (\AA)
1	32.05	0.029	8.50	3.276
2	32.08	0.025	8.09	3.274
3	5.18, 9.81, 13.49	0.012	3.47, 3.68, 1.35	3.270, 3.276, 3.260
4	11.93	0.017	5.06	3.272
5a *	18.68, 8.03, 18.38	0.014	7.36, 2, 4.72	3.274, 3.278, 3.260
5b *	16.25, 14.48, 5.55	0.040	2.09, 3.16, 2.74	3.263, 3.268, 3.277
6	36.10	0.010	8.44	3.263

* Complex **5** crystallizes as two independent molecules, designated **5a** and **5b**.

from **1** and **2** in the identity of the oximate ligand, where Me-saloxH₂ was used in place of saloxH₂. The resulting structural changes in **6** are larger Mn–N–O–Mn torsion angles of $\theta = 36.10^\circ$ and stronger ferromagnetic interactions between Mn^{III} ions (vide infra). In comparison, complex **4** also possesses 3-fold symmetry as a result of its trigonal $R\bar{3}c$ space group, yet shows antiferromagnetic behavior as a result of almost planar salicylaldoximate ligands ($\theta = 11.93^\circ$). The single-ion JT cant angles with respect to the molecular easy axis are also reduced in **4** and can be described by a single tilting axis of $\delta = 5.06^\circ$.

Reduced symmetry analogues have also been synthesized, as seen in complexes **3** and **5**. Complex **3** crystallizes in the monoclinic space group $P2_1/n$, where non-axially symmetric (bent) terminal azido- ligands prevent 3-fold axial symmetry and prohibit the observation of an equilateral Mn₃^{III} triangle. The μ_3 -oxo is displaced just 0.012 \AA out of the Mn₃^{III} plane, while the nearly planar salox²⁻ ligands result in small Mn–O–N–Mn torsion angles ($\theta = 5.18^\circ, 9.81^\circ, 13.49^\circ$) and almost parallel JT axes ($\delta = 3.47^\circ, 3.68^\circ, 1.35^\circ$). The structurally distorted, low-symmetry complex **5** crystallizes in the monoclinic space group $P2_1/c$ as two independent molecules. The first of these molecules has Mn–O–N–Mn torsion angles of $\theta = 18.68^\circ, 8.03^\circ, 18.38^\circ$ and a μ_3 -oxo group displaced 0.014 \AA from the Mn₃^{III} plane. The second molecule has $\theta = 16.25^\circ, 14.48^\circ, 5.55^\circ$ and a 0.040 \AA out-of-plane μ_3 -oxo. Both of these molecules represent a structurally intermediate case between the ferromagnetic complexes that have large θ torsion angles ($>30^\circ$) and the low spin complexes that have small θ torsion angles ($<12^\circ$). Furthermore, crystals of complex **5** contain three disordered [NEt₄]⁺ cations and two MeOH solvate molecules, likely resulting in intermolecular interactions via close molecular contacts and hydrogen-bonding pathways. These structural and crystal packing differences lead to unique magnetic susceptibility and relaxation behavior, as will be described below. Complex **5** is also unique because Zn³ exhibits a highly distorted tetrahedral coordination sphere, with I3–Zn3–N bond angles ranging from 105.33° to 126.44°. Inspection of the crystal packing helps to explain this observation; the relatively short I3...H38 distance of 3.160 \AA would be forced even shorter for a perfectly tetrahedral Zn^{II} ion (Supporting Information, Figure S4).

Direct Current Magnetic Susceptibility Studies. Of the complexes studied, there are two general types of magnetic susceptibility behaviors, the first of which indicates dominant ferromagnetic interactions and the second of which indicates antiferromagnetic interactions. The magnetic susceptibility

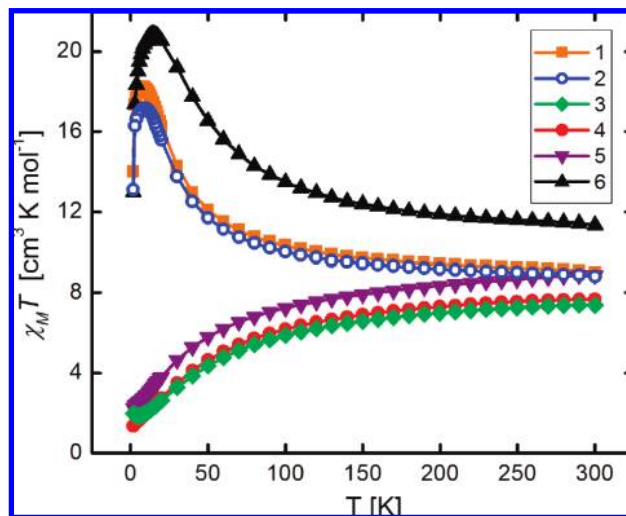


Figure 3. Comparison of $\chi_M T$ data for Cl[−] complexes **1–6** measured at 0.1 T in the range of 1.8–300 K. Solid lines serve as guides for the eyes.

behavior of complexes **1**, **2**, and **6** fall into the former category, as evident by the increase in the value of $\chi_M T$ with decreasing temperature. For complex **1**, the 0.1 T, 300 K $\chi_M T$ value of 9.01 cm³ mol^{−1} K increases gradually as the temperature is decreased, resulting in a value of 12.08 cm³ mol^{−1} K at 50 K. Below 50 K, the value of $\chi_M T$ increases rapidly to a maximum of 18.22 cm³ mol^{−1} K at 7.86 K, followed by a sharp decrease to 14.01 cm³ mol^{−1} K at 1.8 K. The decrease at lower temperatures is attributable to ZFS and Zeeman effects from the applied field. Complex **2** shows virtually identical susceptibility behavior, as expected for this very similar Br[−] analogue. Me-salox²⁻ supported complex **6** exhibits analogous behavior but suggests ferromagnetic interactions that are stronger than in complexes **1** and **2** (Figure 3). Complex **6** has a 0.1 T $\chi_M T$ value of 11.34 cm³ mol^{−1} at 300 K, larger than in complexes **1** and **2**, and also larger than the value of 9.03 cm³ mol^{−1} expected for three uncorrelated $S = 2$ spins. As the temperature is lowered, $\chi_M T$ gradually rises to a value of 13.49 cm³ mol^{−1} K at 100 K. Below this temperature, the susceptibility continues to increase, reaching its maximum of 20.86 cm³ mol^{−1} K at the higher temperature of 14.9 K as compared to complexes **1** and **2**. This value is consistent with an $S = 6$ spin ground state and $g \approx 2$, as expected for a ferromagnetically coupled triangle of Mn^{III} ions. A rapid decrease is observed below 14.9 K, resulting in a $\chi_M T$ value of 12.98 cm³ mol^{−1} K at 1.80 K. These observations follow the geometric trends for these complexes, where larger θ torsion angles in the

structure lead to stronger ferromagnetic interactions and larger corresponding susceptibilities.

The spin-frustrated complex **3** exhibits magnetic susceptibility behavior indicative of dominant antiferromagnetic interactions and possesses a $\chi_{\text{M}}T$ value of $7.38 \text{ cm}^3 \text{ mol}^{-1} \text{ K}$ at 300 K. This value is significantly less than the value of $9.03 \text{ cm}^3 \text{ mol}^{-1}$ expected for three noninteracting high-spin Mn^{III} ions, indicating the presence of antiferromagnetic interactions at 300 K. The value of $\chi_{\text{M}}T$ for **3** decreases smoothly as the temperature is lowered, resulting in a minimum value of $1.85 \text{ cm}^3 \text{ mol}^{-1} \text{ K}$ at 4.83 K. The susceptibility slightly increases below 4.83 K, reaching $1.98 \text{ cm}^3 \text{ mol}^{-1} \text{ K}$ at 1.8 K. These low-temperature data for **3** suggest an apparent spin value of $S = 2$. Complex **4** exhibits similar antiferromagnetic behavior; the 300 K $\chi_{\text{M}}T$ value of $7.67 \text{ cm}^3 \text{ mol}^{-1} \text{ K}$ decreases as the temperature is lowered, reaching a minimum value of $1.35 \text{ cm}^3 \text{ mol}^{-1} \text{ K}$ at 1.8 K. Complex **5** has a slightly larger magnetic susceptibility of 8.87 at 300 K, which decreases to a value of $2.25 \text{ cm}^3 \text{ mol}^{-1} \text{ K}$ at 1.8 K. These data suggest that complexes **3–5** possess antiferromagnetic exchange interactions and low spin ground states.

Studies of Magnetization as a Function of Magnetic Field. Variable-field magnetization data were also collected on complexes **1–6**, taken from 1.8–5.0 K at 1–5 T. These data are shown in Supporting Information, Figures S6–S11 as plots of reduced magnetization ($M/N\mu_{\text{B}}$) versus H/T . Significant zero-field interactions are indicated in all of these complexes, as evident by the non-superimposable isofield curves and magnetization saturation values. The antiferromagnetic complexes **3–5** possess $M/N\mu_{\text{B}}$ saturation values close to 3, which is less than the value of $gS \approx 4$ expected for a Mn^{III} complex with an $S = 2$ spin ground state. In a similar sense, ferromagnetic complexes **1, 2**, and **6** have reduced magnetization values that saturate near 9, somewhat less than $M/N\mu_{\text{B}} = 12.0$ expected for an $S = 6$ complex with $g = 2.0$. These observations are also consistent with non-zero ZFS parameters for complexes **1–6**.

Fitting of dc Susceptibility and Reduced Magnetization Data. Simultaneous fits to the above variable-temperature $\chi_{\text{M}}T$ and variable-field $M/N\mu_{\text{B}}$ magnetization data were accomplished via full matrix diagonalization of the single-ion Hamiltonian given in eq 1. This rigorous approach is absolutely necessary for these complexes, considering the large anisotropy and relatively weak exchange. Attempts to fit the susceptibility data using the van Vleck equation resulted in unreasonable g -values (less than 1.7 or greater than 2.2) and artificially large intramolecular exchange parameters, while attempts to fit the variable-field magnetization data to a single spin ground state resulted in unreasonable g -values ($g \approx 2.2$) and very large axial ZFS parameters ($D \approx -1.7 \text{ K}$). Thus, these results highlight the importance of taking into account *both* the effects of anisotropy and low-lying excited states. A similar effect has been reported for an isotropic ($D = 0$) $\text{Cu}_{17}\text{Mn}_{28}$ cluster, where low-lying

excited-state transitions deceptively suggested a significant anisotropy.³⁷

$$\begin{aligned}\hat{H} &= \hat{H}_{\text{exchange}} + \hat{H}_{\text{zfs}} + \hat{H}_{\text{Zeeman}} \\ \hat{H}_{\text{exchange}} &= -2J_{\text{Mn-Mn}}(\hat{s}_1\hat{s}_2 + \hat{s}_1\hat{s}_3 + \hat{s}_2\hat{s}_3) \\ \hat{H}_{\text{zfs}} &= \sum_{j=1}^3 d \left[\left(\frac{\sin \delta_j}{2} e^{-i\phi_j} \hat{s}_j^+ + \frac{\sin \delta_j}{2} e^{i\phi_j} \hat{s}_j^- + \hat{s}_j^z \cos \delta_j \right)^2 - \frac{1}{3} s_j(s_j + 1) \right] \\ \hat{H}_{\text{Zeeman}} &= g\mu_{\text{B}}\mu_0 \sum_{j=1}^3 (H_x \hat{s}_j^x + H_y \hat{s}_j^y + H_z \hat{s}_j^z)\end{aligned}\quad (1)$$

In eq 1 above, \hat{s}_i represents the total spin operator and $\hat{s}_{\alpha i}$ ($\alpha = x, y, z$) represent the respective components associated with each Mn^{III} ion. Uniaxial ZFS interactions in the local coordinate frame of each Mn^{III} ion are parametrized by d_i (< 0), with δ and ϕ describing the tilting of each Mn^{III} Jahn–Teller axis. The Landé g tensor at each site is parametrized by \vec{g}_i , whereas J_{ij} describes the isotropic exchange couplings between pairs of Mn^{III} ions. For a Mn_3^{III} complex, the dimension of the three spin Hamiltonian matrix is just $[(2s + 1)^3]^2 = 125 \times 125$, which is trivial compared to the $\sim 10^8 \times 10^8$ Hamiltonian matrix for $\text{Mn}_{12}\text{–OAc}$. The single-ion Mn^{III} matrices are further simplified in the C_3 -symmetric Mn_3^{III} examples, as the application of this symmetry operation results in a single exchange constant J_1 . This simplified case is applicable to all of the analogs except for the low symmetry complexes **3** and **5**.

The best fit to the magnetic data for ferromagnetic complex **1** is represented by solid black lines in Figure 4 (top), and corresponds to microscopic spin Hamiltonian parameters of $g = 1.93$, $d = -4.8 \text{ K}$, $J_1 = +2.4 \text{ K}$, and $\delta = 8.43^\circ$. Figure 5 (top) shows the resulting zero-field eigenvalue spectrum for these values, indicating an $S = 6$ ground state and an $S = 5$ first excited spin state. The m_s multiplets corresponding to these spin states are in fact slightly nested, with 0.4 K of overlap between the ($S = 6, m_s = 0$) and ($S = 5, m_s = \pm 5$) states. The energy separation (ΔE) between the ($S = 6, m_s = \pm 6$) and ($S = 5, m_s = \pm 5$) states was also determined for **1** and found to equal 43.3 K. To extract the axial ZFS parameters from these data, the barrier shape for the $S = 6$ ground state was fit to the giant-spin Hamiltonian (eq 2), yielding molecular parameters of $S = 6$, $g = 1.93$, $D = -1.191(1) \text{ K}$ and $B_4^0 = -1.10(3) \times 10^{-4} \text{ K}$. This fit is indicated by the thin red line in Figure 5 (top).

$$\begin{aligned}\hat{H}_{\text{giant-spin}} &= \mu_{\text{B}}B \cdot g \cdot \hat{S} + D \left[\hat{S}_z^2 - \frac{1}{3} S(S + 1) \right] + \\ &B_4^0 \{ 35\hat{S}_z^4 - [30S(S + 1) - 25]\hat{S}_z^2 - 6S(S + 1) + 3S^2(S + 1)^2 \}\end{aligned}\quad (2)$$

The fitting results for complex **2** indicate very similar parameters, as shown in the Supporting Information, Figure S5 and summarized in Table 4. In contrast, the analysis of

(37) Wang, W. G.; Zhou, A. J.; Zhang, W. X.; Tong, M. L.; Chen, X. M.; Nakano, M.; Beedle, C. C.; Hendrickson, D. N. *J. Am. Chem. Soc.* **2007**, *129*, 1014–1015.

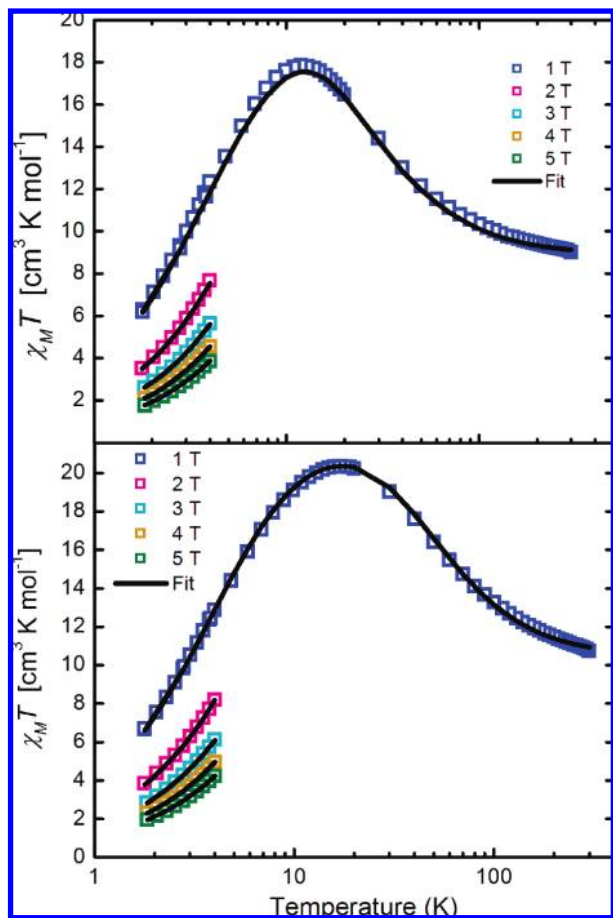


Figure 4. Least-squares fit of the powder magnetic susceptibility data for complexes **1** (top) and **6** (bottom), at 1–5 T from 300–1.8 K. The fit to the microscopic spin Hamiltonian is described by the black lines for the parameters described in the text. Open squares represent the experimental data at the listed fields.

magnetic data for complex **6** reveals differences in comparison to **1** and **2**. The best fit for complex **6** is provided in Figure 4 (bottom) for eq 1 parameters of $g = 2.01$, $d = -4.3$ K, $J_1 = +4.7$ K, $\delta = 8.44^\circ$. Fitting of the ground state to eq 2 resulted in giant-spin parameters of $S = 6$, $D = -1.100(1)$ K and $B_4^0 = -3.75(6) \times 10^{-5}$ K. The most notable comparisons of **6** to complex **1** includes a nearly identical axial anisotropy and a 2-fold increase in magnitude of J_1 , resulting in a more isolated $S = 6$ ground state. Figure 5 (bottom) reveals this clearly, where the ground and first excited-state multiplets in **6** are no longer nested but instead have a 29.0 K separation between the ($S = 6$, $m_s = 0$) and ($S = 5$, $m_s = \pm 5$) states. This also leads to a larger energy separation of $\Delta E = 69.2$ K for the gap between ($S = 6$, $m_s = \pm 6$) and ($S = 5$, $m_s = \pm 5$) states. Additionally, complex **6** has a value of B_4^0 that is nearly one-third that of **1** and **2**. These observations have important implications for explaining the differences in relaxation behavior between **1** and **6**, which will be discussed in detail below.

In contrast to the coupling observed in the above complexes, least-squares fitting of the low-symmetry complex **3** led to optimized single-ion parameters of $g = 2.02$, $d = -8.5$ K, $J_1 = -5.0$ K, $J_2 = -5.0$ K, and $J_3 = -0.1$ K; the corresponding fit is shown as solid black lines in Figure 6 (top). The JT torsion angles of $\delta = 3.28^\circ$, 3.50° , 1.28° and

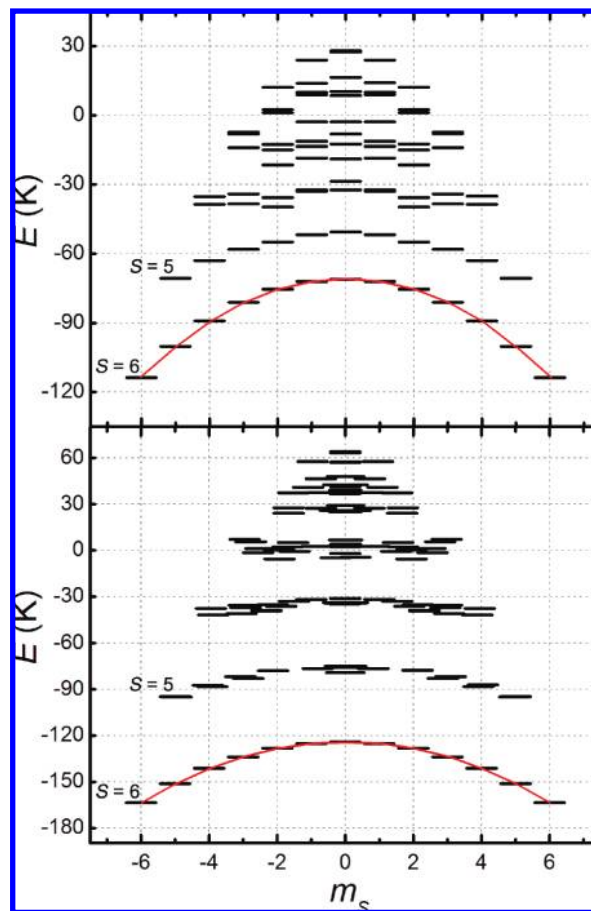


Figure 5. Zero-field eigenvalue spectrum for complexes **1** (top) and **6** (bottom), for parameters discussed in the text.

$\phi = 0^\circ$, 118.69° , 217.32° were taken into account, and were determined from the crystal structure. The second JT torsion angle (ϕ) was necessary for the magnetization data fitting of this complex to account for deviations from C_3 symmetry. Interestingly, the obtained fitting parameters indicate a reasonably isolated $S = 2$ spin ground state ($\Delta E = 35$ K), as observed in Figure 7 (top). Magnetic data for the antiferromagnetic C_3 -symmetric complex **4** were also analyzed in detail, providing the opportunity to compare the effects associated with changes in molecular symmetry. The experimental data for **4** were well fit to eq 1 by the following parameters: $g = 1.94$, $d = -6.2$ K, $J_1 = -4.1$ K, $\delta = 5.06^\circ$, resulting in a highly spin-mixed ground state. The giant-spin Hamiltonian is clearly not appropriate here because of the presence of low-lying excited states. Figure 7 (bottom) describes this visually, where six excited spin states are shown to reside within 7 K of the ground state. This is in contrast to complex **3**, where the first excited-state was determined to lie 35 K above the $S = 2$ ground state. This may be rationalized by considering the geometric relationships between interacting spins in a triangular structure. A high degree of spin frustration exists in a high-symmetry antiferromagnetic triangle, whereas some of this frustration

(38) Feng, P. L.; Beedle, C. C.; Koo, C.; Wernsdorfer, W.; Nakano, M.; Hill, S.; Hendrickson, D. N. *Inorg. Chem.* **2008**, *47*, 3188–3204.

(39) Feng, P. L.; Beedle, C. C.; Koo, C.; Lawrence, J.; Hill, S.; Hendrickson, D. N. *Inorg. Chim. Acta* **2008**, *361*, 3465–3480.

Table 4. Magnetization Fitting Parameters for Complexes 1–4, 6

complex	<i>g</i>	<i>d</i> (K)	<i>J</i> ₁ (K)	<i>J</i> ₂ (K)	<i>J</i> ₃ (K)	δ (deg)	ϕ (deg)	<i>S</i>	<i>D</i> (K)	<i>B</i> ₂ ⁰ (K)
1	1.93	−4.8	2.4			8.43		6	−1.191(1)	$-1.10(3) \times 10^{-4}$
2	1.94	−4.4	2.3			8.09		6	−1.111(1)	$-1.02(3) \times 10^{-4}$
3	2.02	−8.5	−5.0	−5.0	−0.1	3.28, 3.50, 1.28	0.00, 118.69, 217.31	2		
4	1.94	−6.2	−4.1			5.06				
6	2.01	−4.3	4.7			8.44		6	−1.100(2)	$-3.75(6) \times 10^{-5}$

is relieved for a non-equilateral triangle. Thus the observation of a reasonably isolated $S = 2$ ground state in **3** is not surprising considering the low molecular symmetry and weak J_3 exchange parameter. A similar fitting of the magnetic data for complex **5** was not possible, as the presence of two independent molecules results in overparameterization.

Alternating Current Magnetic Susceptibility Studies.

Alternating current susceptibility measurements were performed on ground crystalline samples of complexes **1**–**6**. Comparisons of these ac susceptibility data revealed significant differences in relaxation behavior. The most obvious difference exists between the low-spin complexes **3**–**5** and the ferromagnetic $S = 6$ complexes **1**, **2**, and **6**. Complexes **3** and **4** have very small in-phase susceptibilities ($\approx 1.0 \text{ cm}^3 \text{ mol}^{-1}$ at 1.8 K) and no observable out-of-phase susceptibility in the temperature and frequency range studied. These results are not surprising because of the fast quantum tunneling

processes in complexes **3** and **4**. In complex **3**, the efficiency of QTM is enhanced because of the low molecular symmetry and associated transverse anisotropy. This effect has been well documented, where lower symmetry complexes have been shown to exhibit faster quantum tunneling rates.^{15,38,39}

In complex **4**, the fast magnetic relaxation is of a different origin, namely, the highly spin-mixed ground state arising from the presence of numerous low-lying excited states. The absence of out-of-phase susceptibility signals for complexes **3** and **4** are thus likely because of QTM that is too fast to observe at the operating limits of our SQUID. Complex **5** possesses low frequency χ'_M values that are very similar to **3** and **4**, yet unexpectedly shows measurable out-of-phase susceptibilities (Supporting Information, Figure S12). In fact, at 997 Hz and 1.8 K, the value of χ''_M is approximately 10% of χ'_M . Intermolecular exchange interactions likely contribute to the slow magnetic relaxation in **5**, as numerous close contacts are observed between neighboring molecules. Complex **5** also has two disordered methanol solvate molecules in the unit cell, which may facilitate intermolecular interactions through hydrogen bonds.

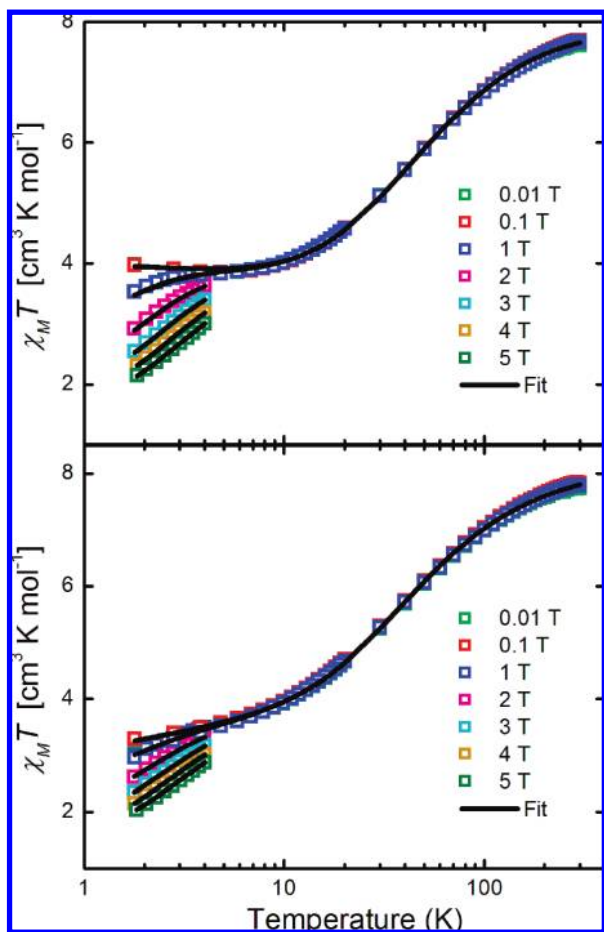


Figure 6. Least-squares fit of the powder magnetic susceptibility data for complexes **3** (top) and **4** (bottom), at 0.01–5 T from 300–1.8 K. The fit to the microscopic spin Hamiltonian is described by the black lines for the parameters described in the text. Open squares represent the experimental data at the listed fields.

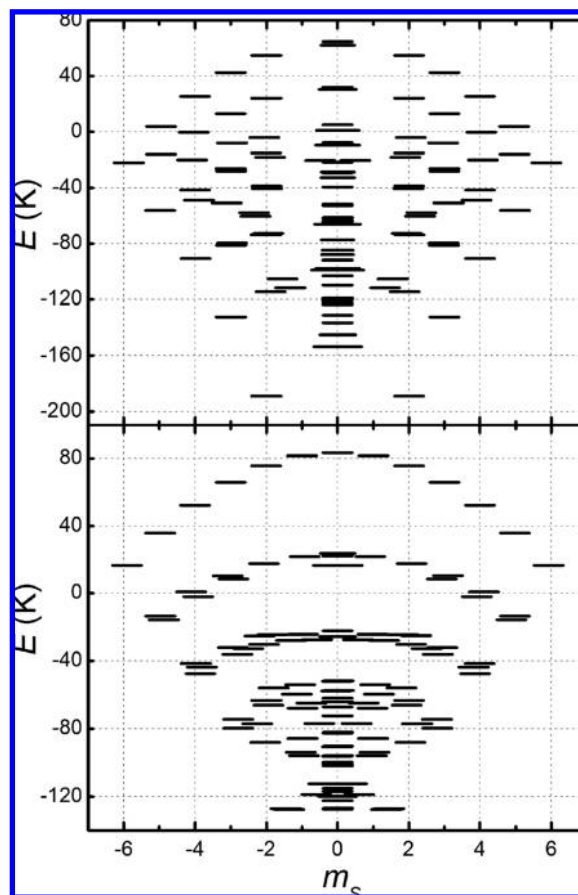


Figure 7. Zero-field eigenvalue spectrum for complexes **3** (top) and **4** (bottom), for parameters discussed in the text.

Table 5. Relaxation Parameters Derived from Fits of the ac Susceptibility Data to the Arrhenius Equation

complex	1	2	6
U_{eff} (K)	44.0	43.7	45.6
τ_0 (s)	3.8×10^{-8}	5.8×10^{-8}	2.1×10^{-7}

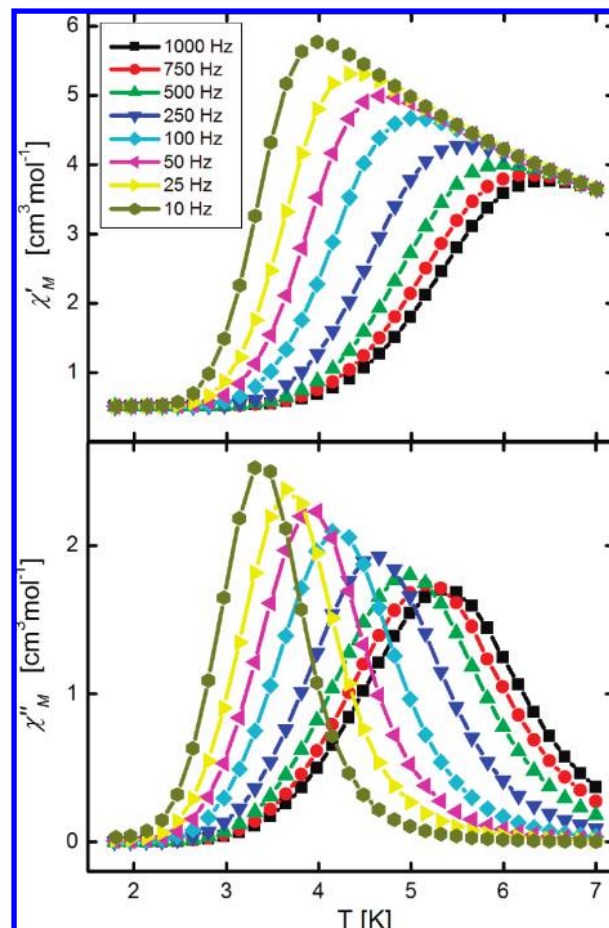
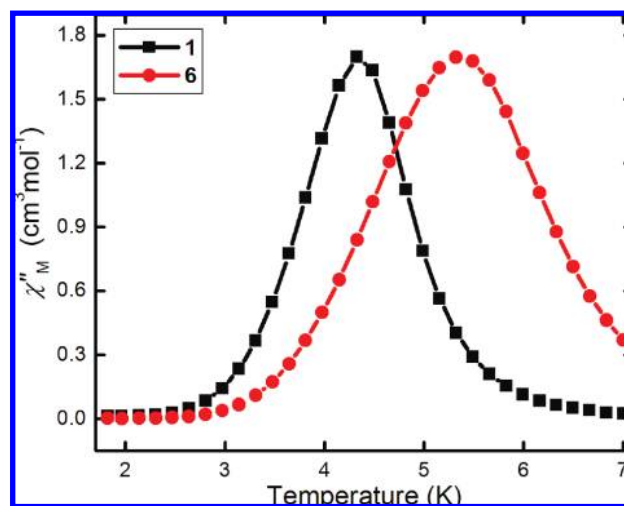
Alternating current susceptibility measurements on the ferromagnetic complexes **1**, **2**, and **6** reveal much different relaxation behavior, where robust frequency-dependent peaks in χ''_{M} are observed (Table 5). Closer inspections of these data also reveal a significant variation of χ''_{M} in the out-of-phase susceptibility, where the out-of-phase peak position has been observed to shift as a result of a change in strength of the ferromagnetic exchange interactions (Figure 8). This result is particularly interesting because it allows for systematic structure-relaxation comparisons to be made. These comparisons are validated, since complexes **1**, **2**, and **6** all crystallize in the trigonal space group $R3c$ and have very similar crystalline packing.

Complexes **1** and **6** have virtually identical formulas of $[\text{NEt}_4]_3[\text{Mn}_3\text{Zn}_2(\text{R-salox})_3\text{O}(\text{N}_3)_6\text{Cl}_2]$, where $\text{R} = \text{H}$ (**1**) or Me (**6**). The out-of-phase ac susceptibility data display well-fit Gaussian peak shapes for both of these complexes, yet show noticeably different peak positions. The 997 Hz χ''_{M} peak position for **1** occurs at 4.32 K, whereas the corresponding peak in complex **6** occurs at 5.36 K (Figure 9). The multi-frequency ac data for these complexes were further analyzed by constructing an Arrhenius plot, as shown in Supporting Information, Figure S15 and described by eq (3) below.

$$\ln(1/\tau) = \ln(1/\tau_0) - U_{\text{eff}}/kT \quad (3)$$

Fitting of the 100–997 Hz χ''_{M} data to this equation resulted in values of $U_{\text{eff}} = 44.0$ K and $\tau_0 = 3.8 \times 10^{-8}$ s for complex **1**, and $U_{\text{eff}} = 45.6$ K and $\tau_0 = 2.1 \times 10^{-7}$ s for complex **6**. Thus, the stronger ferromagnetic interactions in complex **6** not only raises the kinetic barrier by 1.6 K but also results in a 6-fold increase in the value of the pre-exponential factor τ_0 . We rationalize this observation in the context of low-lying excited spin states, where the more isolated ground state in **6** leads to an enhancement in U_{eff} and τ_0 via reduction of relaxation through an excited-state pathway. The optimized (slower) rate of magnetization tunneling in complex **6** is also evident as a reduced zero-field QTM step and larger coercivity at $M/M_s = 0$ in the powder hysteresis loops shown in Supporting Information, Figures S16 (**1**) and S17 (**6**).

High-Frequency Electron Paramagnetic Resonance Studies. Field-orientation-dependent high-frequency electron paramagnetic resonance (HFEP) studies were carried out on single-crystal samples of complexes **1**, **2**, **4**, and **6**. The results for complexes **1** and **2** have been communicated previously.²¹ Meanwhile, complex **6** gives HFEP spectra which are very similar to those of complexes **1** and **2**, as illustrated in Figures 10 and 11, where the field was applied parallel and perpendicular to the easy-axis, respectively. The quality of the spectra obtained for complexes **1**, **2**, and **6** is exceptionally high (narrow resonances), which we attribute to the lack of disordered solvent molecules in their struc-

**Figure 8.** In-phase (top) and out-of-phase (bottom) ac susceptibility for complex **6** from 1.8–7 K at the frequencies shown.**Figure 9.** Comparison of the 997 Hz ac out-of-phase susceptibility (χ''_{M}) data for complexes **1** and **6**.

tures.⁴⁰ Indeed, these spectra are likely the cleanest reported for any SMM, which allows for very precise analysis.

Figure 10b displays a compilation of easy-axis data obtained for complex **6** at many different frequencies, where the data points correspond to the fields at which resonances

(40) Lawrence, J.; Yang, E. C.; Edwards, R.; Olmstead, M. M.; Ramsey, C.; Dalal, N. S.; Gantzel, P. K.; Hill, S.; Hendrickson, D. N. *Inorg. Chem.* **2007**, *47*, 1965–1974.

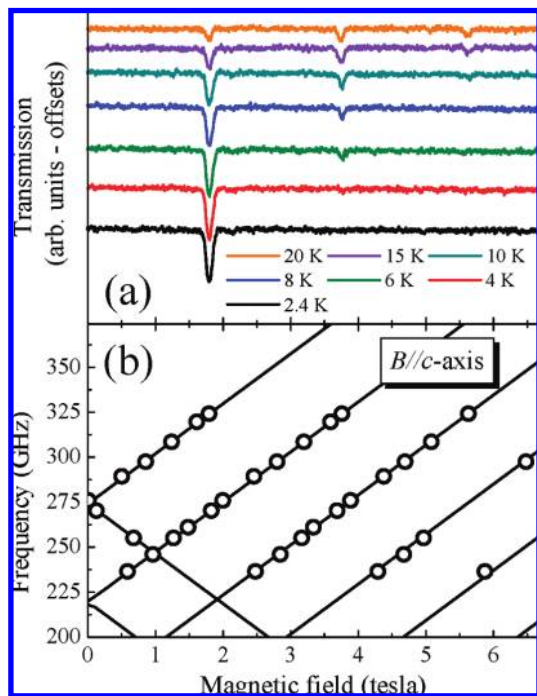


Figure 10. (a) Temperature-dependent EPR spectra for complex **6** at 324.2 GHz, with the magnetic field applied parallel to the easy-axis. (b) Easy-axis EPR peak positions for complex **6** plotted as a function of frequency. The solid lines represent the best simulation of the data using the giant spin Hamiltonian of eq 2. The obtained parameters are listed in Table 6.

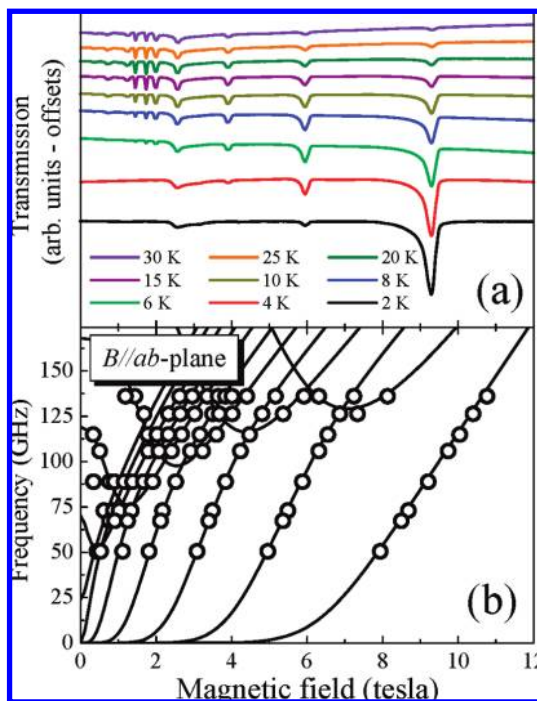


Figure 11. (a) Temperature-dependent EPR spectra for complex **6** at 92.1 GHz, with the magnetic field applied perpendicular to the easy-axis. (b) Hard-plane EPR peak positions at 10 K for complex **6** plotted as a function of frequency. The solid lines represent the best simulation of the data using the giant spin Hamiltonian of eq 2. The obtained parameters are listed in Table 6.

are observed for a particular frequency. High-frequency spectra obtained for this orientation are insensitive to transverse ZFS parameters.⁴¹ Consequently, one may accurately determine the axial parameters D , B_4^0 , and g_z ,

Table 6. ZFS Parameters Obtained via Simulations of HFEPR Data Using the Giant Spin Hamiltonian of eq 2 and the Individual Spin Hamiltonian of eq 1 (see Figures 10 and 11)

complex	S	D (K)	B_4^0 (K)	d (K)	J (K)	g_z	g_x	g_y
1	6	-1.157(7)	$-7.6(1) \times 10^{-5}$	-4.50(7)	2.07(7)	1.97	1.97	1.97
2	6	-1.177(7)	$-7.3(1) \times 10^{-5}$	-4.58(7)	2.26(7)	1.97	1.97	1.97
6	6	-1.163(7)	$-3.6(1) \times 10^{-5}$	-4.39(7)	3.61(7)	1.98	1.98 ^a	1.98 ^a

^a The uncertainties in the Landé factors are ± 0.02 .

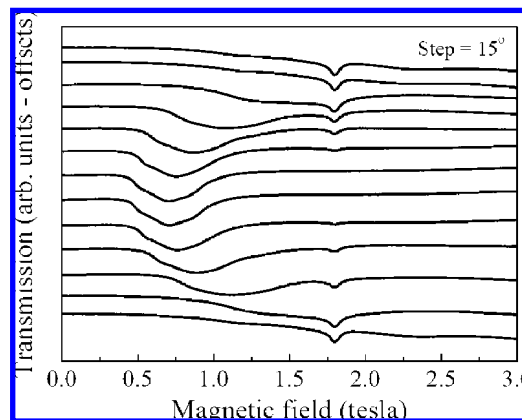


Figure 12. Angle dependent EPR spectra for complex **4** taken at 50.4 GHz and 8 K.

associated with the giant spin Hamiltonian of eq 2. The solid lines in Figure 10b represent the best simulation of the data, and the corresponding parameters are listed in Table 6 along with those obtained for complexes **1** and **2** using the same procedure.²¹

Figure 11 displays hard-plane ($B \perp z$) spectra (a) and simulations (b) for complex **6**. For the simulations, D and B_4^0 were constrained to the values obtained from the easy-axis measurements. Interestingly, no additional transverse ZFS interactions are needed to simulate the hard-plane spectra for complex **6** (only the values of g_x and g_y were adjusted). For complexes **1** and **2**, detailed angle-dependent measurements were performed for field rotations within the hard plane of each crystal. To within the experimental scatter of the data, no detectable modulation of the peak positions was observed, suggesting very weak or non-existent transverse anisotropy. Such measurements were not performed for complex **6**. Nevertheless, we infer very weak transverse ZFS for this complex as well because no additional transverse ZFS parameters were needed for the hard-plane simulations in Figure 11. The giant spin Hamiltonian parameters deduced from these measurements are summarized in Table 6.

Figure 12 displays representative angle-dependent data obtained for complex **4** for field rotations in a plane containing the supposed easy-axis of the crystal. It is immediately apparent that the data are strikingly different to those obtained for the other three complexes; that is, one observes a broad angle-dependent peak with a highly irregular line shape and a sharper angle-independent peak at the isotropic ($g = 2.00$) position. Clearly this difference in behavior is connected with the fact that the interactions in this complex are antiferromagnetic, leading to frustrated

(41) del Barco, E.; Kent, A. D.; Hill, S.; North, J. M.; Dalal, N. S.; Rumberger, E. M.; Hendrickson, D. N.; Chakov, N.; Christou, G. J. *Low Temp. Phys.* **2005**, *140*, 119–174.

spin–spin (superexchange) interactions within the cluster and to many low-lying spin states. Meanwhile, the angle-dependence associated with the broad peak reflects the anisotropy within the cluster originating from the Jahn–Teller distortions on the individual Mn(III) centers. It is impossible to fit these data to any meaningful spin Hamiltonian; that is, the ground state of the cluster does not possess a well defined spin value. However, such findings are entirely consistent with those obtained on the basis of magnetic measurements.

Given the exceptionally high quality of the easy axis data for complexes **1**, **2**, and **6**, it is interesting to assess the validity of the giant spin Hamiltonian which was used to simulate the data in Figures 10 and 11. Inspection of Table 6 indicates that the dominant second order axial parameter (D) is virtually identical for these three complexes. However, the fourth order parameters differ by a factor of 2, that is, $\sim -7.6(1) \times 10^{-5}$ K for complexes **1** and **2** and $-3.6(1) \times 10^{-5}$ K for complex **6**. Our previous studies of tetranuclear Ni(II) complexes have shown that this fourth order anisotropy arises through mixing of spin multiplets;⁴² that is, it is indicative of low-lying spin multiplets and to a breakdown of the rigid giant spin approximation. With this in mind, it is interesting to note that the two complexes with the weaker intramolecular ferromagnetic exchange display the larger B_4^0 values. In other words, complexes **1** and **2** possess smaller exchange coupling parameters, J , leading to lower-lying excited spin multiplets and to greater spin-state mixing. This, in turn, results in the larger B_4^0 values for these two complexes in comparison to complex **6**.

The above suggests that the giant spin approximation may not be the most appropriate description of complexes **1**, **2**, and **6**, as was clearly the case for the antiferromagnetic complex **4**. We can instead use eq 1 to simulate the ZFS within the ground state for each complex. In doing so, one can estimate the intramolecular exchange coupling constants, J , something that was previously thought to be the sole domain of inelastic neutron scattering (INS) spectroscopy.⁴³ The procedure by which we do this is described elsewhere.³⁹ For the present case, we assumed a single exchange parameter, J , and aligned Jahn–Teller axes at the three Mn(III) sites. The obtained single-ion anisotropies (d_i) and molecular J values are included in Table 6 for complexes **1**, **2**, and **6**. It is notable that these are in reasonable agreement with those obtained from fits to the magnetic data obtained using the same Hamiltonian. This may be the first time that EPR and magnetic data have been compared in this way for a family of isostructural complexes, where J is systematically varied without significantly affecting the single-ion anisotropy. Importantly, this work clearly illustrates the interplay between the isotropic (superexchange) and anisotropic (spin–orbit) interactions within the cluster. We note also that very poor agreement would be achieved if one were to use standard methods for analyzing the magnetic data; that is, an isotropic model for fitting the $\chi_{\text{M}}T$ versus T data, and a

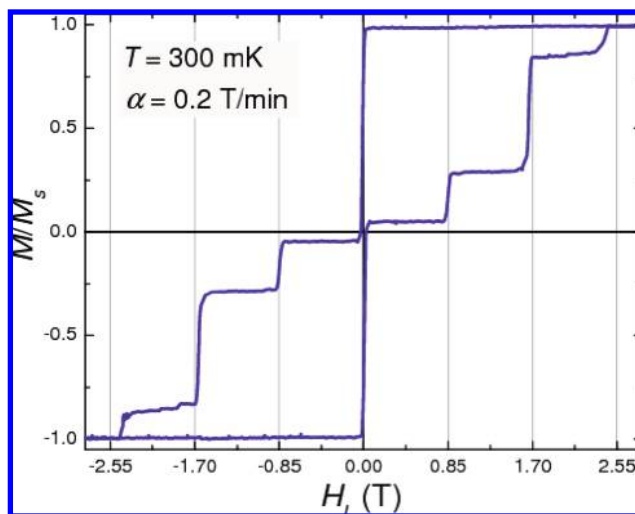


Figure 13. Hysteresis loop recorded at 300 mK in a single crystal of complex **1** with the field applied along the easy axis of the molecules.

giant spin model for fitting the reduced magnetization. Such an approach can only yield reliable parameters in the very few instances in which the exchange and anisotropy scales are very well separated; that is, $J \gg d_i$.

Low Temperature Single Crystal Magnetization Studies. Low temperature magnetization measurements were performed in single crystals of complexes **1** and **2**. Both complexes showed very similar results and can be explained with the same single-ion spin Hamiltonian parameters. In Figure 13 is shown the magnetization hysteresis loop obtained in a $\sim(100)^3 \mu\text{m}^3$ single crystal of complex **1**, recorded at 300 mK by sweeping at a rate of 0.2 T/min a magnetic field applied, H_L , along the easy magnetic axes of the molecules. Sharp steps in the magnetization are observed at 0, ± 0.85 , ± 1.66 , and ± 2.43 T and are attributed to acceleration of the magnetization relaxation because of resonant quantum tunneling, a characteristic fingerprint of a SMM. The same positions of the tunneling resonances were observed in equivalent measurements of a single crystal of complex **2**, as seen in Figure 14, where the field derivatives of magnetization curves obtained at different temperatures are also presented. The results show how the positions of the resonances shift to lower fields when raising the temperature of the measurement, indicating a transition from the pure quantum tunneling regime, in which the relaxation occurs from the ground spin state, to thermally activated tunneling, in which the tunneling occurs through excited states. The fact that the resonances attributed to excited states appear at lower field values is indicative of a fourth order uniaxial anisotropy term in the giant-spin Hamiltonian approximation (i.e., B_4^0 in eq 2), which is ultimately associated to a relatively low exchange interaction constant between the manganese ions in the single ion Hamiltonian (i.e., $J_{\text{Mn-Mn}} \sim d$ in eq 1). The upper graphic in Figure 14 shows the energy levels (continuous lines) obtained by full diagonalization of the single-ion Hamiltonian (eq 1) with the following set of parameters: $s = 2$, $g = 2$, $d = -4.2$ K, $J_1 = +2.44$ K, and $\delta = 8.5^\circ$. The arrows in Figure 14 connect the resonances observed in the experiment with the respective

(42) Wilson, A.; Lawrence, J.; Yang, E. C.; Nakano, M.; Hendrickson, D. N.; Hill, S. *Phys. Rev. B* **2006**, *74*, 140403.

(43) Datta, S.; Waldmann, O.; Kent, A. D.; Milway, V. A.; Thompson, L. K.; Hill, S. *Phys. Rev. B* **2007**, *76*, 052407.

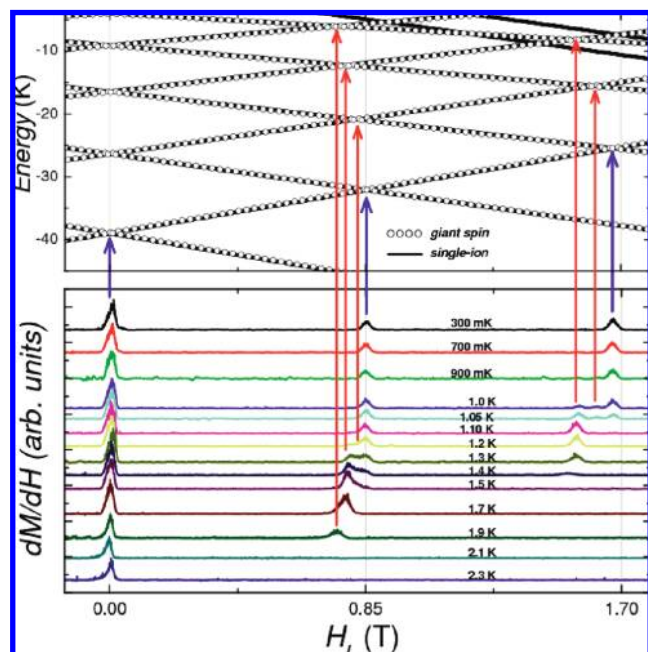


Figure 14. (top) Energy of the spin levels resulting from diagonalization of the single-ion Hamiltonian in eq 1. (lines) and the giant-spin Hamiltonian in eq 2 (open circles). (bottom) Field derivatives of the magnetization curves recorded at different temperatures in complex **2**. Blue arrows mark the resonances observed at low temperatures, when the system relaxes from the ground spin state (pure quantum tunneling regime). Red arrows mark thermally activated quantum tunneling relaxation resonances, whose positions (shifted to lower fields) are determined by the magnitude of the exchange interaction between the manganese ions.

anticrossing of levels at different temperatures. The results are in excellent agreement with the observations obtained from susceptibility, reduced magnetization, and high-frequency EPR spectroscopy studies of these complexes. The results in Figure 14 can also be very well explained by using $S = 6$, $g = 2$, $D = -1.08$ K, and $B_0^4 = -5 \times 10^{-5}$ K in the giant-spin Hamiltonian given in eq 2 (open circles). Consequently, the low temperature magnetization measurements reveal that complexes **1**, **2**, and **6** are SMMs, with total spin $S = 6$ resulting from ferromagnetic exchange interactions between the three manganese ions ($S = 2$) of the molecule.

Conclusion

The diverse magnetic properties within a family of Mn_3Zn_2 complexes have been investigated via bulk magnetic susceptibility, single-crystal HFEPR, and single-crystal magnetization hysteresis measurements. These complexes all

possess planar $[\text{Mn}_3^{\text{III}}-(\mu_3\text{-oxo})]^{7+}$ magnetic cores and have coordinatively identical Mn^{III} environments. Successive changes in the co-crystallizing cation and various coordinating groups have been shown to significantly affect the observed magnetic behavior of these complexes. Spin ground states ranging from a spin-mixed $S \approx 1$ to a reasonably isolated $S = 6$ have been observed as a result of structural perturbations to the core Mn_3^{III} unit, while large axial anisotropies are indicated in each of these complexes. Differences in observed relaxation behavior arise from intermolecular interactions in **5** and changes in the strength of ferromagnetic interactions in $S = 6$ complexes **1** and **6**. The temperature-dependence of QTM resonance positions and HFEPR transitions reveal the effects of intramolecular exchange upon the quantum dynamical behavior, as also indicated by significant differences in ac susceptibility results. Hence, these studies present a step toward better understanding the relaxation behavior of SMMs, through systematic chemical modulation of a series of closely related nanomagnets. Furthermore, the optimized magnetic and relaxation behavior for complex **6** provides valuable insight toward obtaining SMMs with higher blocking temperatures and cleaner quantum behavior, both of which are necessary for future progress in this field.

Acknowledgment. This work was supported by the National Science Foundation (CHE-0714488, DMR-0506946, DMR-0747587). P.L.F. is grateful for a NSF graduate research fellowship (DGE0707423).

Supporting Information Available: Figures S1–S3 (crystal packing diagrams for complexes **1–6**), Figure S4 (molecular representation of complex **5**), Figure S5 (least-squares magnetization fit for complex **2**), Figures S6–S11 (reduced magnetization plots for complexes **1–6**), Figures S12–S14 (ac susceptibility plots for complexes **5**, **1**, and **2**, respectively), Figure S15 (Arrhenius plot for complexes **1** and **6**), Figures S16 and S17 (powder hysteresis loops for complexes **1** and **6**), and Table S1 (BVS values for complexes **1–6**). This material is available free of charge via the Internet at <http://pubs.acs.org>. Atomic coordinates for the respective complexes **1–6** (CCDC 692288, 699692, 699695, 692289, 699694, 711730) have been deposited with the Cambridge Crystallographic Data Centre. The coordinates can be obtained, upon request, from the Director, Cambridge Crystallographic Data Centre, 12 Union Road, Cambridge CB2 1EZ, U.K.

IC802336K